Analyst

PAPER

View Article Online
View Journal | View Issue

Cite this: *Analyst*, 2025, **150**, 3654

Multifunctional terahertz device with angular resilience for biomedical sensing and polarization conversion

Lei Gao,*[a] Taha Sheheryar [b] and Bo Lv*[b]

The demand for high-performance devices capable of both electromagnetic wave manipulation and biomedical detection has intensified with the growth of terahertz technologies. However, most existing devices are designed for a single function, either polarization control or biosensing which limits their utility in integrated systems. Addressing this challenge, we introduce a cost-effective terahertz device that seamlessly integrates broadband cross polarization transformation with precise refractive index sensing, all within a fabrication-friendly structure. Utilizing aluminum patterned resonators on a Rogers RT5870 dielectric layer, the device delivers a polarization conversion ratio above 94% across a wide spectral window of 3.492 THz with peak conversion efficiencies exceeding 99.9% at multiple resonances and retains stable performance at oblique incident angles up to 40°. Simultaneously, it functions as a refractive index sensor reaching a peak sensitivity of 1.35 THz RIU^{-1} and effectively distinguishes between healthy and diseased biological samples including blood, cervical and skin tissues. Compared to state-of-the-art designs which typically specialize in either polarization modulation or biosensing alone, the proposed device stands out for its dual functionality, high sensitivity and ultra-broadband performance. This work fills a rarely addressed research gap by delivering a single device capable of both advanced polarization control and reliable biomedical diagnostics, paving the way for multifunctional terahertz systems.

Received 14th June 2025,
Accepted 10th July 2025

DOI: 10.1039/d5an00646e

rsc.li/analyst

1. Introduction

Precise manipulation of the polarization state of electromagnetic waves is a foundational capability in modern photonic and electromagnetic systems that enables enhanced control over wave propagation, interaction and functionality. Within this domain, metasurface based polarization converters have emerged as highly efficient and compact solutions capable of tailoring wavefronts with subwavelength precision.[1,2] These structures utilize engineered anisotropic resonators to modulate the phase and amplitude of incident fields that allows the conversion of a linearly polarized wave into its orthogonal counterpart through reflection or transmission. Among these, reflective type cross polarization converters are especially advantageous for their planar geometry, exceptional polarization conversion ratios, wide spectral response and resilience to changes in the angle of incidence.[3–5] Their integration into the terahertz frequency regime is especially significant given the unique material interactions and strong field confinement properties available in this spectral window which are vital for the development of compact and high-performance devices. As reported in,[6] a polarization conversion device was introduced with broadband operation from 0.67 to 1.66 THz that achieved an average polarization conversion ratio exceeding 85%. Similarly, another study[7] introduced a photo excited design that achieved PCR values greater than 80% within the 0.65 to 1.58 THz range. These developments reflect the accelerating progress in polarization control technologies and highlight their potential for high efficiency EM modulation.

Building upon the versatility of polarization manipulation, recent research has begun to explore its integration into biosensing technologies leading to the emergence of polarization conversion metasurfaces as viable platforms for highly sensitive, label free detection. Unlike conventional sensing mechanisms that usually depend on absorption measurements or chemical functionalization, polarization based meta sensors operate by detecting minute refractive index variations resulting from biomolecular interactions.[8,9] This method provides several distinct advantages; it enables noninvasive measurement, supports compact and scalable device architectures and accommodates both solid and liquid analytes with minimal sample preparation. When biological specimens interact with

[a]*First Affiliated Hospital, Harbin Medical University, No. 23, Youzheng Street, Nangang District, Harbin 150001, Heilongjiang Province, China. E-mail: gaolei_yida@126.com*
[b]*College of Physics and Optoelectronic Engineering, Harbin Engineering University, Harbin 150001, Heilongjiang Province, China. E-mail: lb19840313@126.com*

the engineered surface of the meta sensor, they induce localized perturbations in the electromagnetic environment which leads to observable shifts in resonant frequency or changes in the reflected polarization state, signals that can be quantitatively linked to biochemical composition.[10] This mechanism has shown strong potential for detecting a range of clinically relevant biomarkers including glucose, hemoglobin and malignant cells. As reported in,[11] a dual function ultrawideband reflective polarization converter achieving a biosensing sensitivity of 1.50 THz RIU^{-1} was introduced which highlights the practical feasibility of integrating polarization conversion and biosensing within a sole design. Yet, despite increasing advancements in each domain, the integration of broadband polarization conversion and high performance biosensing in a unified, multifunctional device remains uncommon. This intersection represents a compelling and largely untapped direction which provides the opportunity to develop compact, general purpose diagnostic tools capable of delivering precise, real-time detection without the need for application specific modifications.

This work proposes a cost-effective terahertz design that combines broad spectrum polarization rotation with precise biosensing capabilities, all integrated into a compact and efficient design. Differing from conventional metasurfaces that rely on complex geometries or expensive materials,[12,13] the proposed structure utilizes Aluminum and Rogers RT5870, both known for their cost efficiency and compatibility with scalable manufacturing processes. The device achieves an impressive average polarization conversion ratio of 98.08% over a broad frequency span of 3.22 THz to 6.802 THz with peak conversion efficiencies exceeding 99.9% at multiple resonances. It sustains a PCR above 94% across a continuous 3.492 THz bandwidth and exhibits a full width at half maximum (FWHM) of 4.194 THz. Notably, the design preserves angular stability and sustains an average polarization conversion ratio of 90.70% at a 40° incidence angle with values consistently above 84% across the entire working spectrum. Beyond its polarization control performance, the design also serves as an efficient biosensing platform that is capable of detecting minute refractive index changes with a maximum sensitivity of 1.35 THz RIU^{-1}. It shows clear discrimination between healthy and pathological tissue in blood, skin and cervical samples and effectively distinguishes malaria infected blood through biologically induced resonance shifts. To date, no reported design has achieved this level of ultrawideband operative bandwidth, high polarization conversion efficiency and integrated biosensing functionality. This work therefore, establishes a promising foundation for next generation terahertz devices capable of advanced polarization control and generalized biomedical diagnostics without the need for disease-specific sensing modules.

2. Design and geometry of the unit cell

The proposed device is designed as a reflective multilayer assembly optimized for broadband polarization conversion and refractive index based biosensing in the terahertz regime. It consists of a patterned aluminum resonator layer deposited on a Rogers RT5870 dielectric substrate and backed by a continuous aluminum ground plane. The substrate with a thickness of 10 μm, relative permittivity of 2.33 and a low loss tangent of 0.0012 provides minimal dielectric loss and effective confinement of the electromagnetic field. The aluminum layers, each 0.1 μm thick with a conductivity of 3.56×10^7 S m^{-1} provides high electrical performance and compatibility with standard microfabrication techniques. The unit cell with a periodicity of 27 μm incorporates an asymmetrically segmented angular loop surrounding a central square patch as shown in Fig. 1. This nonuniform geometry induces strong anisotropy in the surface response that enables the conversion of incident linearly polarized waves into their orthogonal counterparts upon reflection. The geometrical parameters of the resonator are detailed in Table 1 and have been carefully optimized to support wideband operation and efficient polarization conversion.

Fig. 2 shows the operational mechanism where *x* polarized terahertz waves are reflected primarily as *y* polarized waves due to the tailored anisotropic resonance behavior. This cross-polarization arises from the engineered phase discontinuities introduced by the asymmetric resonator layout. Electromagnetic

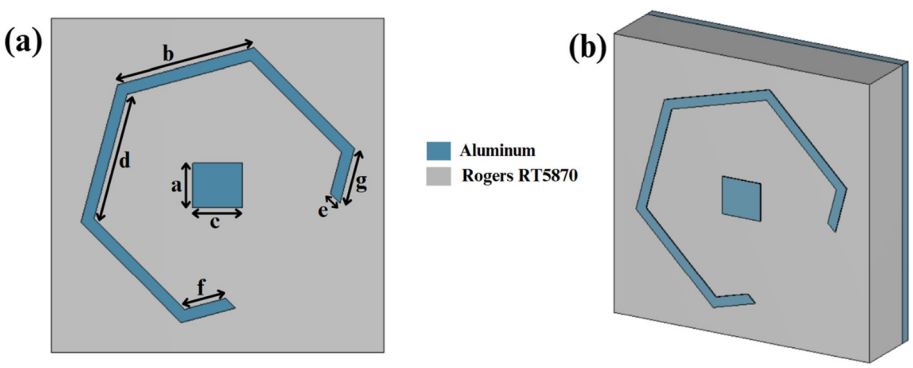

Fig. 1 Schematic of the proposed unit cell structure showing (a) geometric configuration and (b) top view.

Table 1 Geometric dimensions of the unit cell resonator components

Parameters	Values (μm)	Parameters	Values (μm)
a	3.6	*f*	3.47
b	11.5	*g*	4.57
c	4.0	Aluminum	0.1
d	10.4	Rogers RT5870	10
e	1.10	Analyte thickness	04

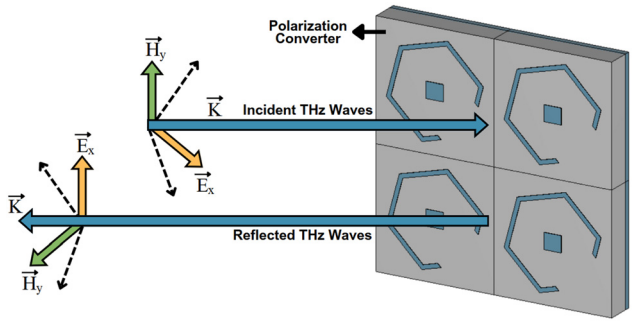

Fig. 2 Illustration of polarization conversion mechanism from incident *x* polarized to reflected *y* polarized wave.

simulations were conducted using CST Microwave Studio with periodic boundary conditions applied along the *x* and *y* axes to emulate an infinite array of unit cells and open boundaries along the z axis to allow wave propagation. A high-resolution mesh comprising over 14 000 tetrahedral elements was used to accurately model the electromagnetic response while more than 5000 optimization sweeps were performed to refine the structural parameters and enhance performance. The resulting design shows excellent polarization conversion efficiency and strong refractive index sensitivity validating its dual functionality as an effective terahertz polarization converter and an integrated biosensing platform.

3. Fabrication process and tolerances

The proposed design can be fabricated using standard photolithography and thin film deposition techniques.[14,15] The process begins by spin-coating a layer of Rogers RT5870 onto a flat surface followed by thermal curing to form a uniform dielectric substrate of 10 μm thickness. A 0.1 μm thick aluminum ground plane is then deposited on the bottom side using e-beam evaporation or sputtering.[16] The top resonator pattern is defined by depositing another 0.1 μm aluminum layer followed by a photoresist application, UV exposure through a mask and development to form the desired pattern.[17] Unwanted metal is removed using a wet or dry etching process finalizing the resonator geometry.[18]

The described fabrication process is compatible with widely used microfabrication techniques and materials. While practical implementation may require adjustment of processing parameters to match simulation conditions, no fundamental obstacles are anticipated. Preliminary prototypes could be developed using standard facilities and experimental work is planned to support the presented results.

4. Performance evaluation

4.1. Analysis of polarization conversion

The polarization response of the proposed structure was assessed through full wave simulation by analyzing the reflection coefficients for orthogonal incident polarizations followed by the calculation of the polarization conversion ratio. Fig. 3 shows the reflection characteristics under *y* polarized excitation. The co polarized reflection coefficient R_{yy} remains suppressed below 0.25 over the entire operating range whereas the cross-polarization component R_{xy} consistently exceeds 0.9 and indicates highly efficient polarization rotation. Similarly, Fig. 4 shows the behavior for *x* polarized incident waves. Here, the co-polarized reflection remains low (max 0.25) and the cross polarized response R_{yx} maintains values above 0.9 that reaffirms strong linear to orthogonal polarization conversion in both excitation modes.

To quantify this efficiency, polarization conversion ratios were computed using the expressions:

$$\mathrm{PCR}_x = \frac{|R_{yx}|^2}{|R_{xx}|^2 + |R_{yx}|^2}, \quad \mathrm{PCR}_y = \frac{|R_{xy}|^2}{|R_{yy}|^2 + |R_{xy}|^2}. \qquad (1)$$

The calculated PCR spectra are plotted in Fig. 5 where both PCR_x and PCR_y exceed 90% across the operational band from 3.22 THz to 6.802 THz. Multiple resonances within this range achieve conversion efficiencies surpassing 99.9%. Furthermore, the structure maintains a Polarization conversion ration above 94% over a continuous 3.492 THz bandwidth with a full width at half maximum of 4.194 THz. These results show the broadband and robust nature of the proposed metasurface design and also its superior polarization conversion performance compared to most existing designs in the terahertz domain.

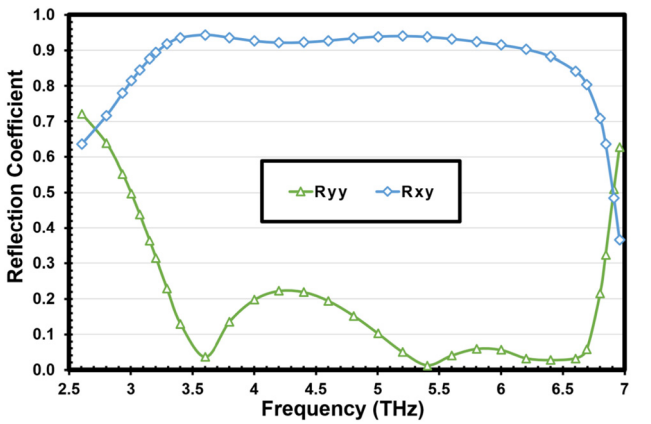

Fig. 3 Reflection coefficients R_{yy} and R_{xy} under *y* polarized incident wave showing strong cross polarization response.

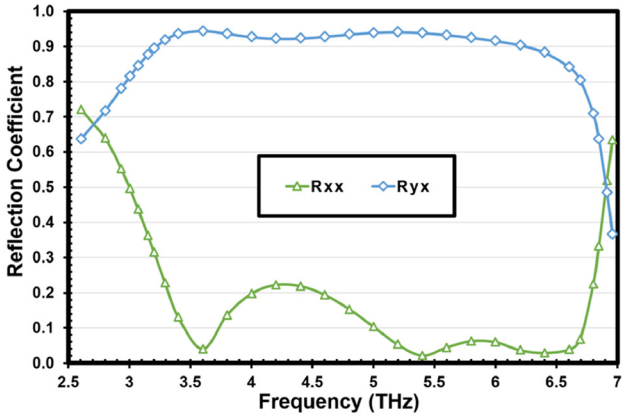

Fig. 4 Reflection coefficients R_{xx} and R_{yx} under x polarized incident wave confirming efficient polarization conversion.

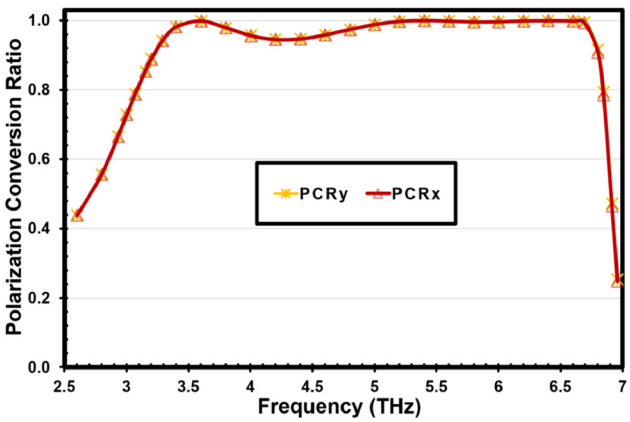

Fig. 5 Polarization conversion ratios PCR_x and PCR_y exceeding 90% across the operating frequency.

4.2. Angular stability

The proposed design's performance under oblique incidence was assessed to determine its angular robustness with results summarized in Fig. 6. Simulations were carried out at incident angles ranging from 0° to 40° to evaluate polarization conversion behavior across varying wavefront orientations. The proposed design consistently demonstrates high stability and maintains an average polarization conversion ratio of approximately 90.70% even at a 40° incidence angle. Notably, the minimum PCR remains above 84% across the evaluated range which underscores the device's resilience under angular deviations. Such robust performance is particularly significant in the terahertz domain where maintaining uniform polarization conversion at larger angles is usually hindered by increased wave dispersion and resonance sensitivity. The observed angular tolerance confirms that the design is well suited for practical terahertz applications where wide-angle operation and consistent electromagnetic response are essential.

To date, no prior work has demonstrated the simultaneous realization of ultra broadband operation, near unity polarization conversion efficiency and robust angular performance especially within the upper terahertz spectrum while also incorporating integrated biosensing capabilities. This level of multifunctional performance is made possible through the deliberate geometric tailoring of the top resonator through optimization sweeps and the strategic selection of cost effective, fabrication-ready materials and therefore marking a significant advancement over existing metasurface technologies.

4.3. Theoretical modeling of polarization conversion mechanism

To provide a comprehensive understanding of the underlying working principles, the polarization behavior of the proposed design is analyzed through a combination of vector decomposition, reflection matrix formulation and phase relationship analysis. Fig. 7 shows the decomposition of electric field components into an alternated reference frame consisting of orthogonal axes u and v each positioned at a 45° angle relative to the traditional Cartesian directions (x and y). This alteration is essential to accurately capture the anisotropic response of the metasurface structure. In this basis, the incident electric field $\vec{E}_i$ is redefined through its projections along the u and v components, formulated as:

$$\vec{E}_i = \hat{u} \cdot \vec{E}_{iu} + \hat{v} \cdot \vec{E}_{iv}. \quad (2)$$

Upon contact with the design, the reflected field component $\vec{E}_r$ is similarly resolved as:

$$\vec{E}_r = \hat{u} \cdot \vec{E}_{ru} + \hat{v} \cdot \vec{E}_{rv}. \quad (3)$$

To model the polarization transformation behavior, the reflection properties are captured using the Jones matrix[19,20] which relates the incident and reflected fields through a 2 × 2 reflection matrix as:

$$\begin{bmatrix} E_{rx} \\ E_{ry} \end{bmatrix} = \begin{bmatrix} r_{xx} & r_{xy} \\ r_{yx} & r_{yy} \end{bmatrix} \cdot \begin{bmatrix} E_{ix} \\ E_{iy} \end{bmatrix}. \quad (4)$$

Here, r_{xx} and r_{yy} are the co polarized reflection coefficients while r_{xy} and r_{yx} denote the cross polarized terms. For an ideal cross polarization converter, the design aims to maximize the cross-polarized reflections $|r_{xy}|^2$ and $|r_{yx}|^2$ while minimizing co-polarized responses $|r_{yy}|^2$, $|r_{xx}|^2$. As shown in Fig. 8, the simulated reflection coefficients R_{uu} and R_{vv} maintain near unity values across the operational band whereas the cross polarized components R_{uv} and R_{vu} remain negligibly small and indicate highly directional and consistent reflection behavior without unintended polarization leakage.

The effectiveness of polarization conversion also depends on the phase relationship between co polarized fields. As depicted in Fig. 9, the phase variations of ϕ_{uu} and ϕ_{vv} is monitored to ensure that the phase difference between them satisfies the key condition for cross polarization:

$$\Delta\phi = |\phi_{uu} - \phi_{vv}| \approx 180°. \quad (5)$$

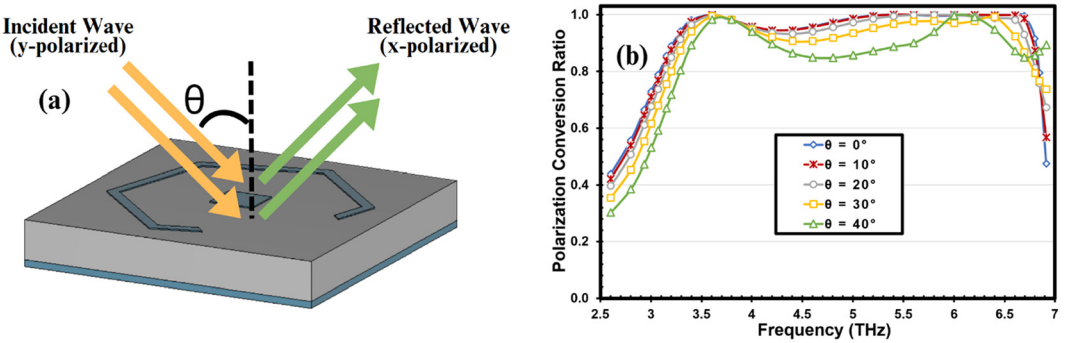

Fig. 6 (a) Schematic illustration of oblique incidence polarization conversion and (b) corresponding performance showing strong angular stability up to 40°.

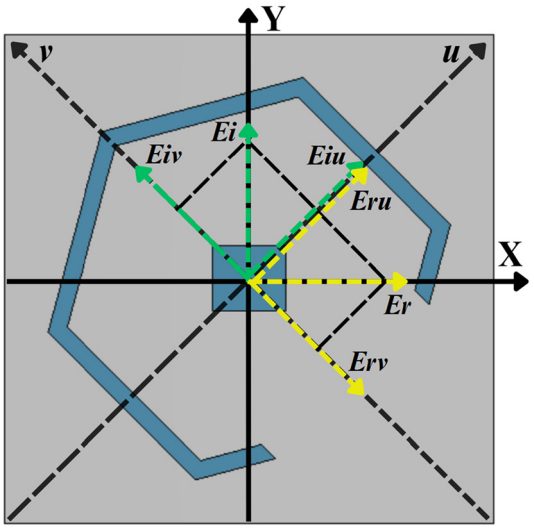

Fig. 7 Field component analysis in the rotated u–v coordinate system.

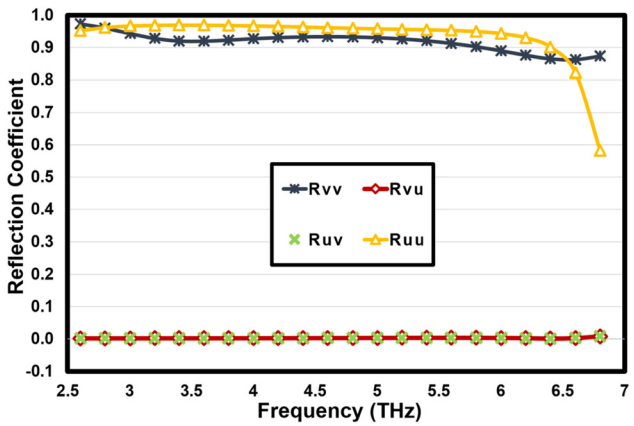

Fig. 8 Numerically evaluated reflection responses in u–v basis showing dominant co polarized response and suppressed cross polarized components.

This phase shift ensures destructive interference in the original polarization direction and constructive enhancement in the orthogonal direction that enables efficient conversion

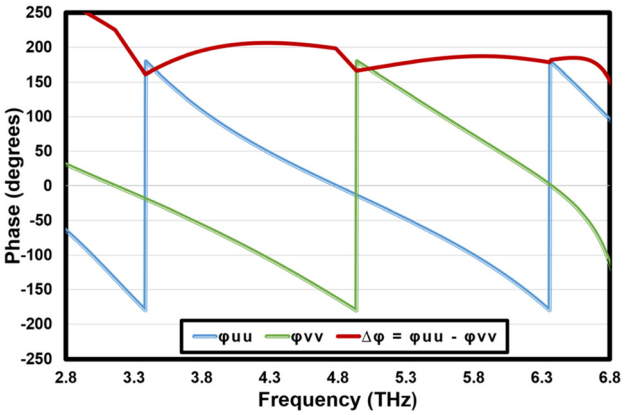

Fig. 9 Phase difference between ϕ_{uu} and ϕ_{vv} demonstrating near 180° shift required for effective polarization conversion.

from linear to cross polarization. The plot clearly shows that this condition is well met across multiple resonances in the operating band. Fig. 10 presents a schematic view of the electromagnetic response of the structure when excited by a y polarized wave. The anisotropic resonator induces resonant field interactions and phase controlled internal reflections within the multilayered structure. As the wave propagates through the structure within an effective medium exhibiting a negative refractive index, constructive buildup of cross polarized reflections and suppression of co polarized components are observed. This interference mechanism contributes to the observed ultra broadband and efficient polarization transformation.

4.4. Surface current distribution

To further understand the polarization conversion phenomenon, surface current distributions were analyzed at two different resonance frequencies *e.g.*, 3.5 Terahertz and 6.5 Terahertz as visible in Fig. 11. In these plots, yellow arrows represent surface currents on the top patterned aluminum layer while blue arrows indicate the corresponding currents on the bottom ground plane. As illustrated in Fig. 11(a), at a frequency of 3.5 THz, the current distribution on large angular

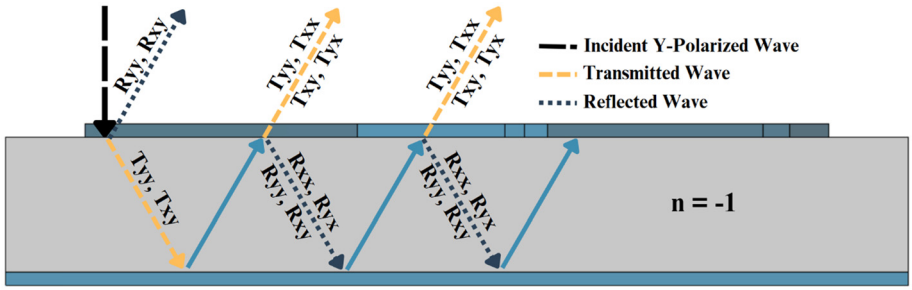

Fig. 10 Schematic illustration of polarization conversion through engineered phase control and resonant reflection in the metasurface.

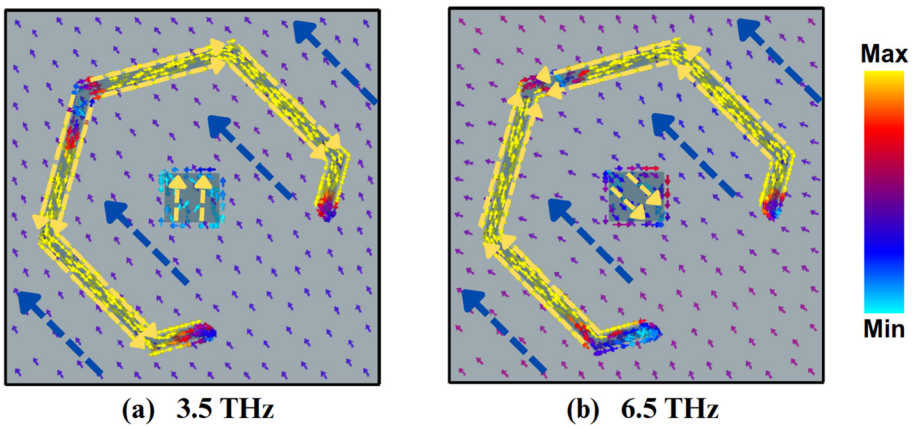

Fig. 11 Surface current circulation at (a) 3.5 THz and (b) 6.5 THz presenting opposing currents between top resonators and ground plane at different regions.

resonator flows in the opposite direction to the current on the bottom metallic layer. This counter flow between top and bottom surfaces is a hallmark of magnetic resonance and is important for achieving efficient polarization rotation. The strong and continuous loop formed around the larger resonator arms promotes the excitation of magnetic dipole moments that drive the polarization conversion process. Fig. 11(b) illustrates a significant redistribution of surface currents at 6.5 THz indicating a shift in the resonant behavior of the structure. Here, the dominant counterflow is observed between the central square patch on the top layer and the bottom ground plane. The current direction in the square patch opposes that of the ground layer directly beneath it and indicate localized resonant activity at higher frequencies. This redistribution of current interaction from the outer loop to the inner patch reflects the design' frequency selective behavior and contributes to maintaining high polarization conversion performance across operating range.

Performance as polarization converter

To comprehensively evaluate the performance of the proposed design, a comparative analysis was conducted against several recently reported polarization conversion designs. The benchmarking focused on key parameters such as operating frequency range, effective bandwidth and polarization conversion ratio, as presented in Table 2. The proposed device shows highly efficient operation over a wide frequency range from 3.220 THz–6.802 THz corresponding to an effective bandwidth of 3.582 THz. Within this span, it maintains a PCR exceeding 94% across a stable interval of 3.292 THz to 6.784 THz resulting in a continuous high-performance bandwidth of 3.492 THz. Furthermore, the design achieves a relative bandwidth of approximately 71.4% and significantly outperforms most existing structures that are typically limited to narrower bandwidths and lower conversion efficiencies. The combination of broadband operation, exceptional polarization conversion and design simplicity underscores the strength of the proposed design as a robust solution for advanced terahertz polarization control applications.

5. Biosensing mechanism and implementation

Beyond polarization control, the proposed design is also engineered to serve as a high sensitivity biosensor that is capable of detecting minute changes in the surrounding dielectric environment. The sensing mechanism uses the strong inter-

Table 2 Performance comparison of the proposed design with existing polarization conversion metasurfaces

Ref.	Unit cell volume	Operating frequency (THz)	Operating bandwidth	Polarization conversion ratio
21	$0.17\lambda_L \times 0.17\lambda_L \times 0.14\lambda_L$	2.15–4.00	1.85 THz	Over 80%
22	$0.23\lambda_L \times 0.23\lambda_L \times 0.08\lambda_L$	0.35–0.65	0.30 THz	—
23	$0.23\lambda_L \times 0.23\lambda_L \times 0.06\lambda_L$	0.65–1.45	0.80 THz	Over 80%
24	$0.10\lambda_L \times 0.10\lambda_L \times 0.10\lambda_L$	0.20–1.00	0.80 THz	Over 80%
25	$0.15\lambda_L \times 0.15\lambda_L \times 0.10\lambda_L$	0.38–1.07	0.69 THz	Over 80%
26	$0.26\lambda_L \times 0.26\lambda_L \times 0.10\lambda_L$	0.20–0.40	0.20 THz	Over 80%
Proposed design	$\mathbf{0.29\lambda_L \times 0.29\lambda_L \times 0.11\lambda_L}$	**3.220–6.802**	**3.582 THz**	**Over 90%**
		3.292–6.784	**3.492 THz**	**Over 94%**

action between incident terahertz waves and the analyte material placed on the surface of the meta structure. As shown in Fig. 12, the experimental setup involves directing a terahertz beam from a source onto the proposed design where the analyte such as a blood sample is deposited directly above the resonator array. The interaction of the terahertz wave with the analyte alters the effective refractive index near the design which in turn perturbs the resonant conditions of the structure. These changes manifest as measurable shifts in the polarization conversion ratio and spectral response. A photodiode detector captures the reflected terahertz signal and transmits it to a computer for spectral analysis. Variations in the analyte composition such as the presence of pathological biomarkers or changes in blood characteristics induce distinct resonance shifts that can be correlated with specific biological states. This non-invasive, label-free sensing approach enables real time monitoring of biofluids and makes the system highly suitable for medical diagnostics and disease detection.

6.1. Refractive index detection mechanism

Fig. 13 shows the polarization conversion ratio spectra for various refractive index values ranging from 1.30 to 1.50. As the refractive index increases, distinct shifts are observed in the PCR curves that shows the design's sensitivity to dielectric changes. Two characteristic resonance points denoted as F_x and F_y are selected from regions where the polarization conversion ration exceeds 90% to ensure high detection fidelity. These points are located on the rising and falling edges of the broadband spectrum where small frequency shifts are most pronounced and easily tracked. To quantify the sensitivity of the biosensor, the following expression is used:

$$S = \frac{\Delta f}{\Delta n}, \tag{6}$$

where S is the sensitivity in THz RIU^{-1}, Δf is the frequency drift and Δn is the alteration in RI. Fig. 14 presents the frequency shift behavior of the selected points F_x and F_y as a function of analyte's RI. A consistent downward trend is visible for both points which indicates that the resonance frequencies decrease as the refractive index increases. This linear and predictable shift shows that both F_x and F_y respond effectively to dielectric variation and also validates their suitability for biosensing applications.

6.2. Biomedical detection and sensitivity evaluation

To demonstrate the real-world applicability of the proposed design as a biosensor, it was evaluated using biologically significant specimens; red blood cells (for malaria detection), HeLa cervical cells and non-melanoma basal skin cells. Each sample type was analyzed under both healthy and diseased conditions with refractive index values sourced from established biomedical literature.[27–38] Variations in refractive index between normal and pathological states resulted in measurable frequency shifts at designated sensing points F_x and F_y. As summarized in Table 3, disease conditions such as malaria, cervical cancer and skin cancer produced distinct spectral

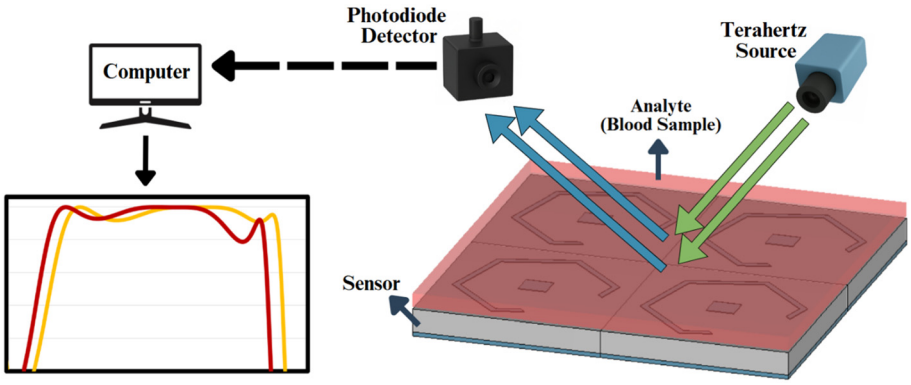

Fig. 12 Schematic of the biosensing setup showing terahertz excitation, analyte placement over the sensor and detection of resonance shifts due to refractive index changes.

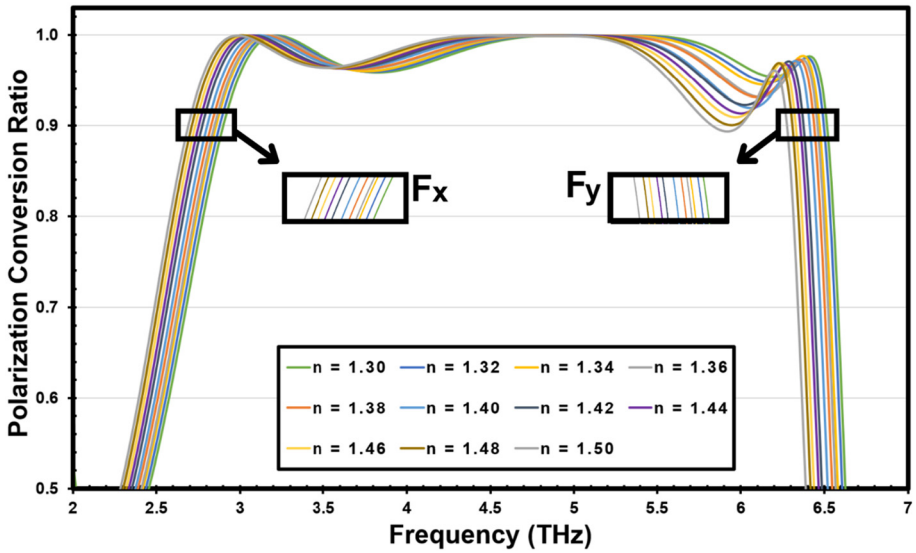

Fig. 13 PCR spectra for varying refractive indices (1.30–1.50) showing resonance shifts; two high-sensitivity points are marked above the 90% polarization conversion threshold.

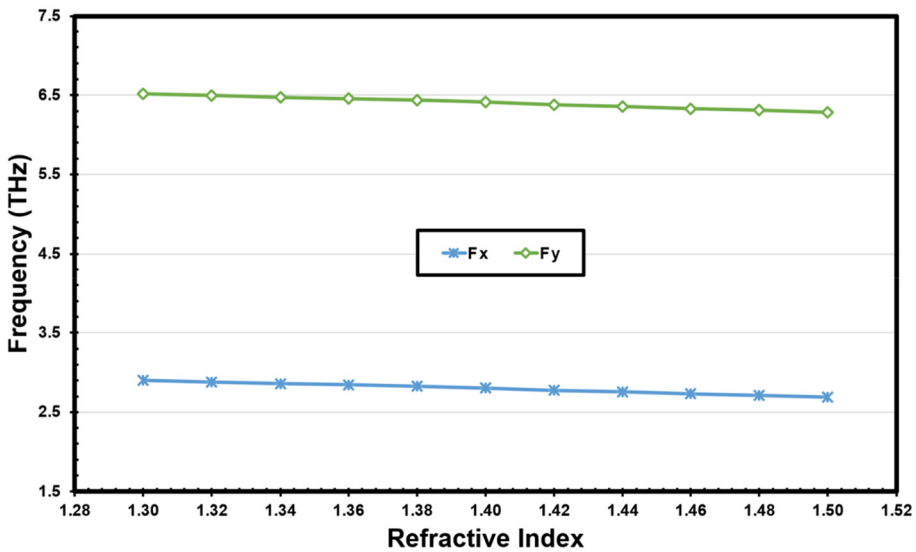

Fig. 14 Frequency shifts at points F_x and F_y *versus* refractive index demonstrating a downward trend and showing reliable sensitivity to dielectric changes.

Table 3 Refractive index values, resonant frequency shifts and calculated sensitivities for healthy and diseased biological samples at designated sensing points F_x and F_y

Sample	Type	State	Refractive index	F_x	Sensitivity (F_x)	F_y	Sensitivity (F_y)
Blood	Red blood cells	Healthy	1.399	2.805	1.11	6.413	1.23
		Malaria	1.373	2.834		6.445	
Cervical	HeLa cell	Healthy	1.368	2.839	1.04	6.452	1.25
		Cancerous	1.392	2.814		6.422	
Non-melanoma skin	Basal cell	Healthy	1.36	2.846	1.05	6.458	1.35
		Cancerous	1.38	2.825		6.431	

Table 4 Performance comparison of the proposed dual functional biosensor with recent state-of-the-art designs in terms of sensitivity, materials and application scope

Ref.	Applications	Unit cell volume (μm)	Materials	Sensitivity (THz RIU^{-1})	Year published
39	RI sensor	94 × 94 × 65	Gold-silicon	0.28	2020
40	Transmitter	90 × 90 × 16	Gold-quartz	0.28	2021
41	Reflector	300 × 300 × 350	Cupper-quartz	0.05	2022
42	Absorber	100 × 100 × 8.6	Gold-GaAs	0.08	2023
20	Bio sensor	20 × 20 × 4.2	Gold-polyimide	0.68	2024
43	Bio sensor	12 × 12 × 6.36	Gold-polyimide	0.95	2025
Proposed work	Multi-disease sensor	27 × 27 × 10.2	Al-Rogers RT5870	1.35	—

shifts with the resonant frequencies moving in accordance with minute RI differences. For example, malaria-infected blood (RI = 1.373) showed a higher F_x shift compared to healthy blood (RI = 1.399) corresponding to a sensitivity of 1.11 THz RIU^{-1} at F_x and 1.23 THz RIU^{-1} at F_y. Similarly, for cervical cells, the metasurface recorded sensitivities of 1.04 THz RIU^{-1} and 1.25 THz RIU^{-1} for F_x and F_y respectively. The highest sensitivity (1.35 THz RIU^{-1}) was observed in the F_y mode for skin samples. These results not only show the biosensor's ability to differentiate between healthy and abnormal tissue but also demonstrate its balanced dual-polarization conversion response.

The proposed approach demonstrates sensitivity suitable for distinguishing relevant sample conditions. In applied scenarios, various factors such as handling practices or local environmental variations could have some influence on detection results. Depending on specific application requirements, additional methods like surface preparation or optional integration with microfluidic systems may be explored to tailor selectivity and operational consistency as needed.

6. Comparative evaluation with existing metasurface biosensors

To assess the relative performance of the proposed sensor, a comparison was conducted with several recent metasurface based designs reported in literature. Key parameters such as application type, unit cell volume, material composition and sensitivity are summarized in Table 4. Most of the referenced works focus exclusively on single purpose biosensing usually optimized for either refractive index detection, transmission modulation or absorption enhancement. These designs usually lack polarization manipulation capability and are limited to specific diagnostic targets.

In contrast, the proposed design stands out by combining ultra-wideband polarization conversion and extremely sensitive sensing in a single, fabrication-friendly device. Achieving a peak performance of 1.35 THz RIU^{-1}, it surpasses all previously existing values in the comparison including high end biosensors based on gold-polyimide structures. Additionally, while other designs employ noble metals like gold or bulky unit cell architectures, the proposed sensor uses cost-effective metal and substrate to enhance practical scalability. Importantly, very few existing works, if any, simultaneously support broadband polarization control and biosensing within the same architecture. This distinct capability not only broadens the operational scope of the sensor but also reduces the need for multiple dedicated platforms. The proposed design therefore presents a significant advancement as a multi-disease diagnostic metasurface with superior electromagnetic and biomedical performance.

7. Conclusion

This study presents a compact terahertz structure capable of concurrently achieving broadband polarization rotation and sensitive biosensing performance within a single, multifunctional and fabrication-friendly design. Constructed using aluminum resonators on a Rogers RT5870 substrate, the structure achieves a high average polarization conversion ratio of 98.08% sustaining values above 94% across a continuous 3.492 THz bandwidth. The design maintains stable performance under oblique incidence up to 40% with performance remaining above 84% throughout the operational range. In addition to its electromagnetic response, the proposed design exhibits strong biosensing performance with refractive index sensitivity reaching up to 1.35 THz RIU^{-1}. It successfully differentiates between healthy and pathological conditions in blood, cervical and skin samples by tracking resonance shifts at dual sensing points. Performance benchmarking against existing works shows that very few reported designs achieve this level of integration with most limited to either biosensing or polarization control. The proposed work addresses this gap by delivering both functionalities within a single, scalable platform. The outcomes of this study establish the design as a promising candidate for advanced terahertz applications especially in label-free biomedical diagnostics and polarization sensitive electromagnetic systems.

Author contributions

The research presented in this manuscript is the outcome of joint contributions from all authors. Lei Gao carried out the full wave simulations and analytical evaluations with technical support from Taha Sheheryar and Bo Lv. The first draft of the manuscript was composed by Lei Gao with revisions and

enhancements led by Bo Lv. Each author actively contributed to the development of the final version and approved it for publication.

Conflicts of interest

The authors declare no competing interests.

Data availability

All results generated and analyzed in this research are fully presented within the final issued version.

Acknowledgements

L. G. was sponsored by The Scientific Research and Innovation Fund of the First Affiliated Hospital of Harbin Medical University, 2020B10; Research Project of Health Commission of Heilongjiang Province, 2020-139. B. L. was sponsored by the National Natural Science Foundation of China under Grant No. 61901133; Fundamental Research Funds for the Central Universities 3072024XX2504; Forward Design Technology Special Fund Project of Harbin Engineering University KYWZ220242504, KYWZ220240807; Heilongjiang Provincial Key Research and Development Program 2024ZX01A09.

References

1 A. Ahmad and D.-Y. Choi, Design, optimization, and comparative analysis of wide-band polarization conversion along with dual coding sequences for RCS reduction, *Sci. Rep.*, 2024, **14**(1), 8262.
2 Q. Zheng, C. Guo and J. Ding, Wideband metasurface-based reflective polarization converter for linear-to-linear and linear-to-circular polarization conversion, *IEEE Antennas Wireless Propag. Lett.*, 2018, **17**(8), 1459–1463.
3 H.-T. Chen, A. J. Taylor and N. Yu, A review of metasurfaces: physics and applications, *Rep. Prog. Phys.*, 2016, **79**(7), 076401.
4 R. Dutta, J. Ghosh, Z. Yang and X. Zhang, Multi-band multi-functional metasurface-based reflective polarization converter for linear and circular polarizations, *IEEE Access*, 2021, **9**, 152738–152748.
5 Z. Xiao, *et al.*, A tunable reflective polarization converter based on hybrid metamaterial, *Opt. Quantum Electron.*, 2017, **49**, 1–11.
6 R. Xia, *et al.*, Broadband terahertz half-wave plate based on anisotropic polarization conversion metamaterials, *Opt. Mater. Express*, 2017, **7**(3), 977–988.
7 J. Zhao, Y. Cheng and Z. Cheng, Design of a Photo-Excited Switchable Broadband Reflective Linear Polarization Conversion Metasurface for Terahertz Waves, *IEEE Photonics J.*, 2018, **10**(1), 1–10.
8 V. Naresh and N. Lee, A review on biosensors and recent development of nanostructured materials-enabled biosensors, *Sensors*, 2021, **21**(4), 1109.
9 B. Kaur, S. Kumar and B. K. Kaushik, Recent advancements in optical biosensors for cancer detection, *Biosens. Bioelectron.*, 2022, **197**, 113805.
10 M. Gezimati and G. Singh, Terahertz cancer imaging and sensing: open research challenges and opportunities, *Opt. Quantum Electron.*, 2023, **55**(8), 727.
11 T. Sheheryar, F. Waqar, B. Lv and L. Gao, An ultra-wideband terahertz linear cross-polarization converter with integrated biosensing for multi-disease diagnosis, *J. Mater. Chem. C*, 2025, **13**(24), 12460–12471.
12 H. Bi, M. Yang and R. You, Advances in terahertz metasurface graphene for biosensing and application, *Discover Nano*, 2023, **18**(1), 63.
13 T. Sheheryar, *et al.*, A graphene-based tunable polarization insensitive terahertz metasurface absorber for multi-band high-efficiency applications, *J. Mater. Chem. C*, 2025, **13**(11), 5545–5554.
14 H. R. Seren, *et al.*, Optically modulated multiband terahertz perfect absorber, *Adv. Opt. Mater.*, 2014, **2(12)**, 1221–1226.
15 H.-T. Chen, *et al.*, Active terahertz metamaterial devices, *Nature*, 2006, **444**(7119), 597–600.
16 H. Tao, *et al.*, Highly flexible wide angle of incidence terahertz metamaterial absorber: Design, fabrication, and characterization, *Phys. Rev. B: Condens. Matter Mater. Phys.*, 2008, **78**(24), 241103.
17 N.-H. Shen, *et al.*, Optically implemented broadband blueshift switch in the terahertz regime, *Phys. Rev. Lett.*, 2011, **106**(3), 037403.
18 X. Liu, *et al.*, Laser etching of aluminum thin film on polyimide: Simulation and experimental studies, *Surf. Coat. Technol.*, 2015, **277**, 107–116.
19 M. I. Khan, *et al.*, Multiband linear and circular polarization rotating metasurface based on multiple plasmonic resonances for C, X and K band applications, *Sci. Rep.*, 2020, **10**(1), 17981.
20 V. Maurya and S. Singhal, Dual band terahertz reflective linear cross polarization converter-based biosensor, *IEEE Sens. J.*, 2024, **24**(5), 6103–6110.
21 Y. Cheng, *et al.*, Terahertz broadband tunable reflective cross-polarization convertor based on complementary cross-shaped graphene metasurface, *Phys. E*, 2021, **134**, 114893.
22 B. Yin, Z. Xu and Y. Ma, Terahertz off-axis focus polarization converter based on metasurface, *Prog. Electromagn. Res. Lett.*, 2021, **100**, 91–97.
23 Y. Z. Cheng, *et al.*, Ultrabroadband reflective polarization convertor for terahertz waves, *Appl. Phys. Lett.*, 2014, **105**(18), 181111.
24 R. T. Ako, *et al.*, Ultra-wideband tri-layer transmissive linear polarization converter for terahertz waves, *APL Photonics*, 2020, **5**(4), 046101.
25 R. T. Ako, *et al.*, Broadband and wide-angle reflective linear polarization converter for terahertz waves, *APL Photonics*, 2019, **4**(9), 096104.

26 J.-S. Li and F.-Q. Bai, Dual-band terahertz polarization converter with high-efficiency asymmetric transmission, *Opt. Mater. Express*, 2020, **10(8)**, 1853–1861.
27 S. K. Patel, J. Surve and J. Parmar, Detection of cancer with graphene metasurface-based highly efficient sensors, *Diamond Relat. Mater.*, 2022, **129**, 109367.
28 T. Sheheryar, Y. Tian, B. Lv and L. Gao, Transforming medical diagnostics with metasurface terahertz biosensing technology: a label-free biosensor for detecting multiple diseases, *Opt. Quantum Electron.*, 2025, **57**(5), 280.
29 T. Parvin, K. Ahmed, A. M. Alatwi and A. N. Z. Rashed, Differential optical absorption spectroscopy-based refractive index sensor for cancer cell detection, *Opt. Rev.*, 2021, **28**, 134–143.
30 S. Banerjee, *et al.*, A theoretical terahertz metamaterial absorber structure with a high quality factor using two circular ring resonators for biomedical sensing, *Inventions*, 2021, **6**(4), 78.
31 T. Sheheryar, Y. Tian, B. Lv and L. Gao, High-sensitivity refractive index based terahertz metasurface biosensor for detecting multiple cancers and infectious diseases, *Photonics Nanostruct. Fundam. Appl.*, 2025, **65**, 101399.
32 R. Khan, *et al.*, Refractive index of biological tissues: Review, measurement techniques, and applications, *Photodiagn. Photodyn. Ther.*, 2021, **33**, 102192.
33 P. Upender and A. Kumar, Ultrathin, ultra narrow band DMMA for biosensing applications, *IEEE Trans. NanoBiosci.*, 2022, **22**(3), 529–537.
34 T. Sheheryar, Y. Tian, B. Lv and L. Gao, Highly Sensitive Polarization-Independent Metasurface Terahertz Biosensor for Multi-disease Diagnosis, *Plasmonics*, 2025, DOI: **10.1007/s11468-025-02903-x**.
35 V. Maurya and S. Singhal, Ultrathin Multiband Polarization-Independent Terahertz Absorber as a Biosensor, *IEEE Sens. J.*, 2023, **23(21)**, 25919–25926.
36 B. Lv, T. Sheheryar, J. Wekalao and L. Gao, Ultra-wideband and angular-stable Terahertz reflective cross-polarization converter integrated with highly sensitive biosensing, *Mater. Res. Bull.*, 2026, **193**, 113641.
37 X. Huang and B. Wang, High sensitivity terahertz sensor based on semiconductor material for biosensing detection, *J. Mater. Chem. C*, 2025, **13**(10), 5148–5160.
38 S. S. Birunda, H. Subramani, A. K. Udayakumar and T. Sheheryar, Machine Learning-Enhanced Terahertz Biosensor with Mxene-Graphene Conjugate for High-Sensitivity Malaria Detection, *Plasmonics*, 2025, DOI: **10.1007/s11468-025-03152-8**.
39 T. Chen, *et al.*, Design of a terahertz metamaterial sensor based on split ring resonator nested square ring resonator, *Mater. Res. Express*, 2020, **7**(9), 095802.
40 L. Zhu, *et al.*, Dual-band electromagnetically induced transparency (EIT) terahertz metamaterial sensor, *Opt. Mater. Express*, 2021, **11(7)**, 2109–2121.
41 G. Deng, *et al.*, A Metamaterial-Based Absorber for Liquid Sensing in Terahertz Regime, *IEEE Sens. J.*, 2022, **22**(22), 21659–21665.
42 S. Anwar and M. Khan, High-performance terahertz refractive index sensor for cancer cells detection, *Eur. Phys. J. E: Soft Matter Biol. Phys.*, 2023, **46**(3), 19.
43 V. Maurya and S. Singhal, Ultrathin reflecting wideband terahertz cross polarization converter as a biosensor, *Mater. Res. Bull.*, 2025, **185**, 113292.